Future Sustainability
Open Access Journal
ISSN 2995-0473

February 2024| Volume 02 | Issue 01 | Pages 01-13

Journal homepage: https://fupubco.com/fusus

https://doi.org/10.55670/fpll.fusus.2.1.1

Future Publishing LLC

Article

# Microstructured pebble stone like Ni-NiO composite as anode of high-performance lithium-ion batteries

**Safina-E-Tahura Siddiqui[1], Md. Arafat Rahman[1]*, Md. Saiful Islam[2], Jin-Hyuk Kim[3], Nirjhor Barua[1]**

[1]Department of Mechanical Engineering, Chittagong University of Engineering and Technology, Chittagong-4349, Bangladesh
[2]Department of Glass and Ceramic Engineering, Bangladesh University of Engineering and Technology, Dhaka, Bangladesh
[3]Clean Energy R&D Department, Korea Institute of Industrial Technology, 89 Yangdaegiro-gil, Ipjang-myeon, Seobuk-gu, Cheonan-si, Chungcheongnam-do, 31056, Republic of Korea

**ARTICLE INFO**

*Article history:*
Received 10 September 2023
Received in revised form
14 October 2023
Accepted 27 October 2023

Keywords:
Thermal oxidation, NiO, Composite, Anode, LIBs

*Corresponding author
Email address:
arafat@cuet.ac.bd

DOI: 10.55670/fpll.fusus.2.1.1

**ABSTRACT**

Ni-NiO electrodes were synthesized via thermal oxidation of pure nickel powder and evaluated as anode of lithium-ion batteries (LIBs). The composite synthesized at 600˚C, 800˚C, and 1000˚C exhibited nanochips, crushed gravel stone, and pebble stone-like morphology, respectively. The nanochips- and crushed gravel stone featured-like electrodes exhibited erratic behavior, and specific capacity faded rapidly from 754.49 mAh $g^{-1}$ and 101.12 mAh $g^{-1}$ to 464.04 mAh $g^{-1}$ and 9.55 mAh $g^{-1}$, respectively over 10$^{th}$ cycle at a current rate of 1C as the electrode experiences internal short circuit. The pebble stone-like Ni-NiO electrode exhibited improved and stable cyclic performance with 1$^{st}$ discharge capacity of 365.17 mAh $g^{-1}$ and reduced to 67.42 mAh $g^{-1}$ even after 40$^{th}$ cycle at 1C current rate. The improved electrochemical performance of composite Ni-NiO with a pebble stone-like feature can be attributed to the mechanical stability of the electrode, which can buffer volume expansion, and the presence of more nanoparticles on the electrode surface allows more interaction with $Li^+$.

## 1. Introduction

Lithium-ion batteries (LIBs) have acquired immense attention and popularity as rechargeable batteries for portable consumer electronics applications due to high gravimetric and volumetric energy density, zero memory effect, and low self-discharge rate [1]. Besides consumer electronics, LIBs are being employed in aerospace, military applications, grid energy storage, electric vehicles (EV), hybrid electric vehicles (HEV), and plug-in hybrid electric vehicles (PHEV) [1–4]. The implication of these batteries is that they mitigate the environmental pollution resulting from the burning of fossil fuels [5]. It is noted that graphite is employed as an anode in commercial LIBs as it is inexpensive, has high reversibility during the charge/discharge process, and has excellent stability. However, its cycling capacity is restricted due to possessing low theoretical capacity (372 mAh $g^{-1}$) [6,7], which cannot fulfill the market demand for next-generation rechargeable LIBs. Moreover, graphite anode experiences extensive structural deterioration upon cycling that leads to drastic capacity fading; high polarization initiates lithium dendrite formation and low operating voltage [8]. From that quest, establishing a favorable anode material with high capacity, environmentally benign, and rate performance is very crucial to advancing the performance of LIBs [9–12]. In addition, pure alloys as LIB anodes face some issues, for instance, volume expansion and electrode fracturing during the lithiation process, which causes mechanical fracture of active electrode particles, resulting in electrical detachment and capacity fade and unstable SEI formation [13–15]. However, titanium-based oxides are investigated as the anode; it can eradicate the issues regarding alloy anodes with a long cycle life since it has no SEI and just a 1% volume change. Unfortunately, with a 1.5V versus Li/$Li^+$ operating voltage, as well as a limiting specific

capacity of 160 Ah $kg^{-1}$, the battery energy density is reduced [16]. Among all anode materials, Transition metal oxides (TMOs) are recognized as the most suitable anode materials for LIB due to their high theoretical capacity, natural affluence, eco-friendly nature, cost-effective fabrication procedure, and chemically durable [17–23]. Moreover, TMOs as anode material eliminate the problem of lithium dendrite formation, safety issues, and low specific capacity. It is noted that TMOs encounter some issues, such as rapid capacity depletion due to volume-induced strain during electrochemical cycling, resulting in intense polarization and electrode pulverization [24–27]. To address these issues, nanostructured TMOs are being employed because of their large electrode/electrolyte contact area, short diffusion length, and efficient strain accommodation [28,29]. NiO is a competitive candidate among other TMOs and is explored widely as an alternative electrode material for high-performance LIBs due to its high theoretic capacity of 718 mAh $g^{-1}$, cost-effectiveness, environment benignity, and natural abundance [30]. The density of NiO is 6.81 g $cm^{-3}$, which is three times higher as compared with graphite of 2.26 g $cm^{-3}$. The theoretical energy density of NiO is about 5.8 times higher than graphite [31]. Nevertheless, the practical application of NiO in LIBs is still obstructed because of its excessive volume variation and destruction of the active electrode material, as well as poor ionic conductivity, which results in poor electrochemical performance [32, 33]. To alleviate these issues, various morphologies of NiO are studied to analyze electrochemical performance, for instance, porous, mesoporous structures [36], nanocomposite [31, 37, 38], nanogravel [23], nanosheets [39, 40], nanowalls [41], nanofibers [42], hollow nanotubes [43], nanofilms [44], nanowires [45], hierarchical structures [46–50], nanocone array [51], composited with carbon [52–55] or conductive polymers [56,57] have been investigated, which in comparison to graphite and pure NiO exhibited improved electrochemical performance. In addition, several strategies such as hydrothermal, microwave hydrothermal, co-precipitation, sol-gel method, pyrogenation, solvothermal, chemical emersion, spray pyrolysis, powder metallurgy and annealing is adopted to fabricate different NiO nanostructures [58,59]. Among these strategies, thermal oxidation of Ni powder is considered a facile and cost-effective process, which can be adapted to synthesize unique morphological structures. Numerous investigations were carried out regarding electrochemical performance evaluation of NiO synthesized through thermal oxidation [31, 51, 60, 61]. In some studies, NiO was combined with carbon to form composites, which exhibit excellent cycling stability [62–64]. However, the composite synthesis process is tedious and the existence of low-density carbon greatly reduces the volumetric specific capacity. In addition, the inclusion of high-density metals can contribute to enhancing electrochemical performances [65,66]. Huang et al. prepared Ni-NiO nanocomposite through calcination in a tube furnace at $700^0$C [66]. The nanocomposite constitutes <10 nm of Ni particles and 100 nm of NiO particles. The enhanced electrochemical performance of electrodes due to the presence of the metallic Ni phase facilitates a more reversible reaction during the charging process. Comparatively, strong polarization was monitored owing to the presence of crystal defects. The rate capability and cycling performance were not satisfactory due to the slow kinetics of NiO particles and the transportation of electrons. Therefore, considerable research is required to be done to acquire stable cycling performance and rate capability of NiO as LIB anode material. In this specific study, we synthesized microstructured composite of Ni-NiO through a single-step thermal oxidation process and mechanical ball milling. The composite structures were employed as anodes and provided efficient electrolyte access throughout the structure, which resulted in high discharge capacity and excellent cycling performance. In addition, the synthesized composite electrode exhibited different morphology at different oxidation temperatures. The presence of the metallic Ni phase facilitates the reverse decomposition process and improves electrical conductivity. It can be foreseen as a high-performance LIB electrode.

## 2. Experimental

### 2.1 Synthesis of Ni-NiO nanocomposite

The composite Ni-NiO fabrication involves a single-step thermal oxidation process in an electric furnace (Nabertherm, USA) at three distinct temperatures, as shown in Figure 1.

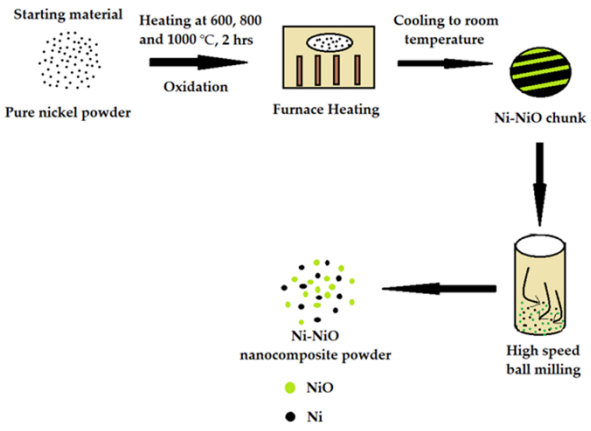


**Figure 1.** Schematic representation of Ni-NiO composite synthesis process

Thermal oxidation is the method of growing a thin oxide layer on the surface of a wafer, which follows Wagner's theory, as shown in Figure 2. The commercially available Ni powder (99.8% purity, maximum limit of impurities are Iron (Fe): 0.01%, Sulphur (S): 0.001%, Carbon (C): 0.08%, Oxygen (O): 0.15 %) of 20 gram was heated at $600^0$C, $800^0$C, and $1000^0$C in the furnace for 2 hours. The oxidation of Ni powder was above $500^0$C [41,67]; hence, at the above temperatures, nickel was oxidized to NiO. The NiO film growth on the Ni powder surface was initiated via a step increase in the temperature of oxidation in the air. The samples were kept for day-long, and this cooling process was naturally inside the furnace after finishing the oxidation process. The product of thermal oxidation, a greenish NiO layer formed on the surface of Ni, which was mainly a chunk of Ni-NiO. The mass of the nickel powder before and after oxidation was measured using a precision electronic balance machine (SCIENTECH Inc.,

USA) with a readability of 0.001 mg. The chunk of Ni-NiO nanocomposite was ball-milled into the cylinder of the ball milling machine, which was filled with crushed oxidized particles and balls of two diameters in a 10:1 ratio. During the process of collision between balls and crushed particles, the particles got crushed, the size of the particles was reduced, and the ultimate composite powder of Ni-NiO was formed. The crushed particles were then strained to achieve a smooth and homogeneous composite powder.

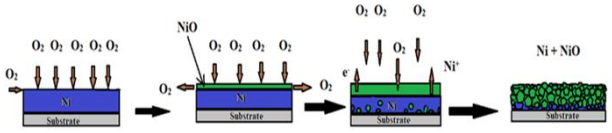


**Figure 2.** Schematic representation of the thermal oxidation process

### 2.2 Characterization techniques

An X-ray diffractometer (XRD) (Empyrean, PANalytical-Netherlands) with radiation from the copper target (kα, λ=0.15406 nm) was used to evaluate the crystal structure and composition of the Ni-NiO crystal structure. The diffraction patterns were recorded over a 2θ range from 10 to $90^0$ at a step size of $0.1^0$. The morphology and structure of the nanocomposite Ni-NiO sample were examined using a high-resolution scanning electron microscope (SEM) (JSM 7600F, JEOL-Japan) in combination with Energy Dispersive X-ray Spectroscopy (EDX) at 5 KV with different magnification.

### 2.3 Electrochemical Measurements

The synthesized and characterized nanostructured composites of Ni-NiO were employed as an anode of LIBs. The electrochemical performance of the synthesized anode was carried out by assembling the electrode into a CR2032-type coin cell (supplied by Xiamen TOB New Energy Technology Ltd., China) in the laboratory. The synthesized nanocomposites of Ni-NiO were used as working electrodes prepared through a slurry coating procedure, as shown in Figure 3. It is noted that the slurry constituted 70 wt. % of active material, 10 wt. % of polyvinylidene fluoride (PVDF) binder, and 20 wt. % of active carbon powder, which was dissolved in the required amount of N-methyl pyrrolidone (NMP) (Sigma-Aldrich). The prepared slurries were then pasted onto a copper foil (Changzhou DLX Alloy Co., Ltd., China). The counter electrode was recycled $LiCoO_2$, and a porous polymeric separator of polyethylene was employed. The electrolyte was $LiPF_6$ (supplied by Ximen $T_{max}$ Battery Equipment Ltd., China) of 1.0 M dissolved in ethylene carbonate (EC) and diethylene carbonate (DEC) at a volume ratio of 1:1. The assembled coin cells were crimped at 100 psi pressure using a hydraulic battery crimper (Metrology Laboratory, Dept. of ME, CUET). The galvanostatic charge/discharge tests were performed using a LAND-CT2001A (LANDt Instrument, USA) battery testing system in a voltage range between 0.02 to 3 V at a 1C current rate.

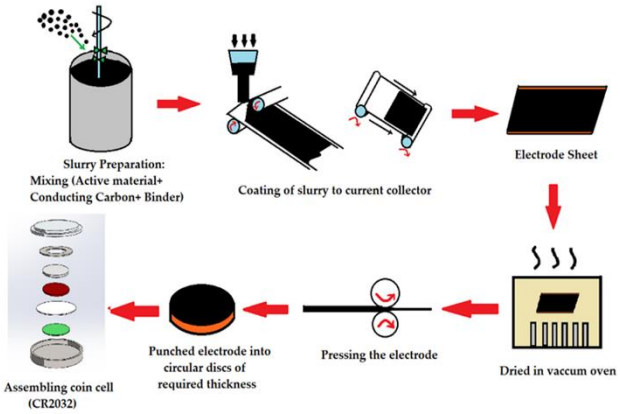


**Figure 3.** Schematic view of composite electrode preparation and coin cell assembly

## 3. Results and Discussions

### 3.1 Characterization of nanocomposite Ni-NiO as an anode of LIBs

Figure 4 shows the XRD pattern of Ni-NiO nanocomposite at different oxidation temperatures, such as 600̊ C, 800̊ C, and 1000̊ C, respectively. To compare with the pure Ni, the XRD pattern of pure Ni is shown. The XRD pattern of pure Ni powder reveals that a face-centered cubic (FCC) structure with three main diffraction peaks at 44.54˚, 51.92˚, 76.46˚ corresponding to the (111), (200), and (202) miller indices of Ni (ICSD: 98-064-6085). The absence of any kind of impurity phases within the detection limit of the diffractometer confirms the purity of Ni powder. In addition, despite the oxidation of Ni at three distinct oxidation temperatures, no other diffraction peaks corresponding to the oxide phase are detected. It is noted that the XRD pattern of Ni shows high intensity and sharp peaks.

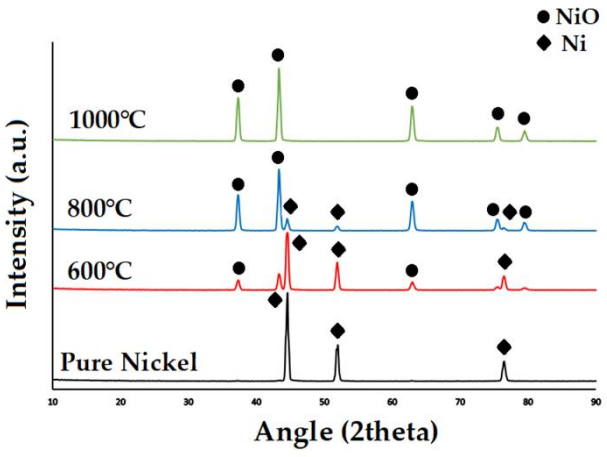


**Figure 4.** XRD pattern of Ni-NiO composite after single-step thermal oxidation at 600˚C, 800˚C, and 1000˚C.

At 600℃ C oxidation temperature, Ni (ICSD: 98-064-6092) exhibited three peaks at approximately the same 2θ angle with five additional diffraction peaks at 37.31˚, 43.35˚, 62.97˚, 75.49˚, 79.51˚, which reveals the formation of NiO (ICSD: 98-002-8834). These peaks can be indexed to the (111), (200), (202), (311), and (222) diffraction planes. In addition, Ni (ICSD: 98-064-6089) and NiO (ICSD: 98-018-4918) peaks are observed with an increase in peak intensity of NiO and a decrease in diffraction peak of Ni due to the thermal oxidation of Ni powder at 800℃ C. It is noted that more oxidation of Ni with increasing temperature and the NiO peaks become sharp with temperature rise which indicates the degree of crystallinity increase of NiO particles. At the oxidation temperature of 1000℃ C, there are no obvious peaks of Ni, the diffraction peaks of NiO (ICSD: 98-018-4918) are observed with high intensity and sharp peaks, as shown in Figure 4. The major sharpening of peaks, mainly of 2θ = 37.31˚, 43.35˚, 62.97˚ indicates the increased degree of crystallization [68]. The crystallographic parameters of Ni-NiO composite at different oxidation temperatures were determined by the Debey Scherrer equation,

$$D = 0.94\,\lambda / (\beta\cos\theta) \quad (1)$$

where D denotes the average dimension of crystallites, λ denotes the wavelength of X-ray, and β denotes the full width at half maximum of a reflation located at 2θ.

The average crystal size of pure Ni before oxidation was 19.93 nm, and after oxidation at 600$^0$C and 800$^0$C is 19.77 nm and 18.13 nm, respectively. However, there is no visible Ni peak at the temperature of 1000℃ C. It is noted that, with the increase in oxidation temperature, the crystal size of Ni decreases. In contrast, five diffraction peaks of NiO at 600℃ C were found at 2θ = 37.31˚, 43.35˚, 62.97˚, 75.49˚, and 79.51˚ with an average crystal size of 17.13 nm while at 800℃ C and 1000˚C, same five NiO peaks exhibited with average crystal size of 18.72 nm and 18.86 nm, respectively. Hence, the crystal size of NiO increases with an increase in oxidation temperature. The possible reason for the increasing crystallite size of NiO is due to oxidation, which leads to more NiO formation. A similar phenomenon was observed as the crystallite size of the metal oxides exhibited an increment with an increase in temperature until it achieved a constant crystal size [68]. Figure 5 shows the low- and high-magnification images of Ni powder before and after oxidation at 600$^0$C. The SEM of pure Ni, as shown in Figures 5 (a) and (b), revealed that the particles are spherical in shape as well as partially agglomerated and smooth, and there are spaces in between the particles. However, this powder was oxidized in the electric furnace at 600˚C continuously for 2 hours; the growth of oxide particles occurs in between the spaces because of the swelling of grains. A significantly different morphology was observed of Ni powder after oxidation in the furnace at 600˚C. The as-synthesized Ni-NiO composite showed a randomly ordered interconnected “nanochips” like structure, as shown in Figures 5 (c), (d), due to the formation of NiO in Ni powder. At a low oxidation temperature of 600˚C, no obvious grain boundary was found, however, the oxide layer growth occurs due to oxidation. A rough surface was formed, which is seen in the high magnification SEM image of the surface, as shown in Figure 5 (d), due to oxide growth. The EDX spectrum confirms the presence of only the Ni phase before oxidation, both Ni and O phases after oxidation, as shown in Figures 5 (e) and (f).

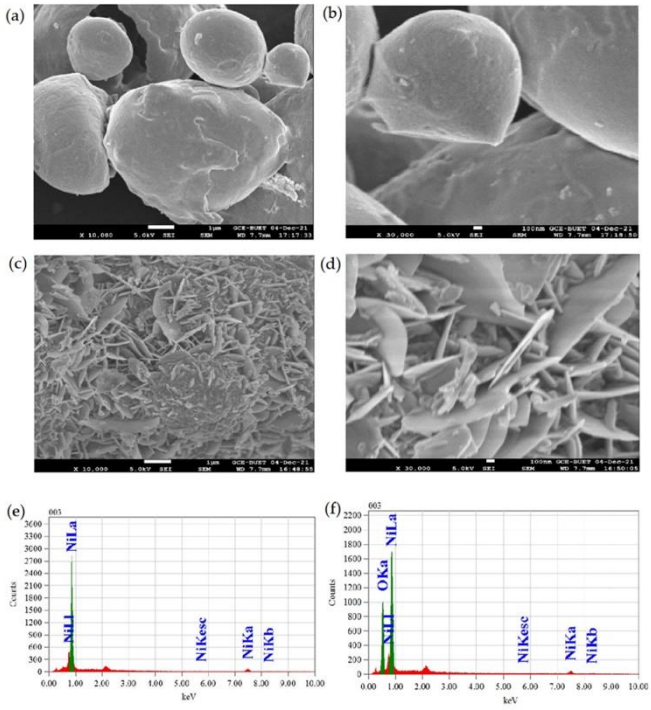


**Figure 5.** Low and high magnification SEM images and EDX spectra of Ni powder: (a), (b), (e) pure nickel powder, and (c), (d), (f) after oxidation at 600˚C

Figure 6 shows low and high-magnification SEM images of nickel powder after oxidation at 800˚C and 1000˚C temperatures. At 800˚C oxidation temperature, the increased grain swelling causes the grain contact area to enlarge, which is responsible for the intergranular joint formation [69]. It is noted that the grains are bonded well as more NiO is formed when compared to the sample oxidized at 600˚C, and grain boundary is formed as shown in Figures 6 (a), (b). As the temperature of oxidation increases, more oxygen is diffused through the porosity of the sample [70,71]; hence, more NiO is formed in the structure. The surface exhibited a “crushed gravel stone” like morphology with a 0.855 µm average grain size. It is noted that there are some cracks and spaces in between the grains due to the diffusion of nickel as well as induced thermal stress. These kinds of cracks and spaces suggest that $Li^+$ transportation could take place easily because of the access of electrolytes through them. Figures 6 (c) and (d) represent the low and high-magnification SEM images of nickel powder after oxidation at 1000˚C temperature. The grains are well interconnected with each other as the swelling of grains due to the oxidation process causes them to fill up the intergranular spaces. The high magnification image of the structure, as shown in Figure 6 (d) reveals that there are no visible pores or voids in the

structure and it exhibits a "pebble stone" like feature with a mean diameter of 0.899 µm which is quite different from the other two oxidized samples. The generation of different thermal stress is the main reason for different morphology at different temperatures [72]. At $1000^0$C oxidation temperature, a visibly smooth surface is observed in the high magnification image, as shown in Figure 6 (d).

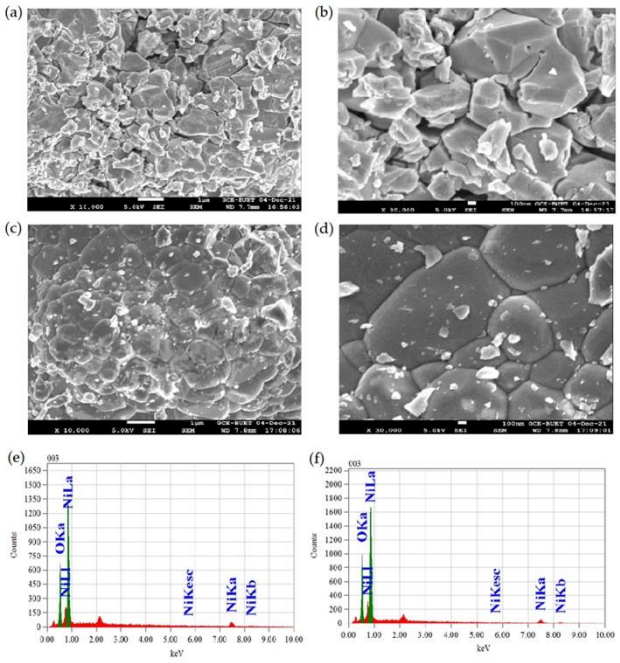


**Figure 6.** Low and high magnification SEM images and EDX spectra of Ni powder: after oxidation at (a), (b), (e) at 800˚C, and (c), (d), (f) at 1000˚C

The EDX spectra exhibited that there are both nickel (Ni) and oxygen (O) is present, which confirms the formation of the NiO phase in the synthesized composite structures. During EDX measurement different areas were focused, and the corresponding peaks are shown in Figures 6 (e) and (f). It is noted that every spectrum confirms the presence of the Ni and O phases.

### 3.2 Electrochemical performance of Ni-NiO composite as anode of LIBs

The electrochemical performances of synthesized Ni-NiO composites were evaluated to assess their efficiency as anodes for LIB. The performance evaluation was accomplished by comparing the galvanostatic charge-discharge profile for different composite anodes to figure out the effect of oxidation temperature on the battery performance. In this study, three types of batteries are assembled employing three kinds of composite. These three batteries are assembled by exerting- microchips ($600^0$C, B-1), crushed gravel-stone ($800^0$C, B-2), and pebble stone ($1000^0$C, B-3) structured negative electrodes. It is noted that NiO is a conversion reaction-based anode that captures lithium possessing high specific capacities by reversibly replacing redox reactions within $Li^+$ and transition oxide-based cation. The elementary conversion reaction mechanism of NiO can be given as $NiO + 2Li^+ + 2e^- \leftrightarrow Ni + Li_2O$. During the discharge phase, NiO is reduced to highly dispersed metallic Ni nanoparticles and $Li_2O$. In addition, the disintegration of $Li_2O$ and the reformation of metallic Ni nanoparticles into NiO nanograins take place during the charge phase.

#### 3.2.1 Electrochemical performance of Ni-NiO composite at $600^0$C and $800^0$C as anode of LIBs

The galvanostatic charge-discharge voltage profiles within a potential window of 0.01-3.0V versus $Li^+$ with cyclic performance and coulombic efficiency for the B-1 and B-2 batteries (synthesis temperature of $600^0$C and $800^0$C) at a current rate of 1C is shown in Figures 7 (a)-(d). It is noted that the 1C rate signifies the accomplishment of charge/discharge in an hour. For battery B-1, the 1st cycle charge-discharge capacity was observed to be 754.49 mAh $g^{-1}$ and 464.04 mAh $g^{-1}$ with 61.50% coulombic efficiency. In addition, the B-1 battery delivered charge-discharge capacities of 23.59 mAh $g^{-1}$ and 11.79 mAh $g^{-1}$; 10.11 mAh $g^{-1}$, and 10.67 mAh $g^{-1}$ at the 5th and 10th cycles, respectively. The consecutive coulombic efficiencies were observed to be 52.5% and 95%, respectively. In contrast, the capacities were 101.12 mAh $g^{-1}$ and 79.78 mAh $g^{-1}$, with a coulombic efficiency of 127.46%, for battery B-2. In addition, the battery B-2 exhibited 5th and 10th cycle charge-discharge capacities of 25.28 mAh $g^{-1}$ and 28.09 mAh $g^{-1}$; 7.30 mAh $g^{-1}$ and 9.55 mAh $g^{-1}$, respectively. The coulombic efficiency was observed as 111.11% and 130.77%, respectively. It is noted that the capacity exhibited drastic decay with cycling as cycled both batteries. In addition, only 2.29% of the initial discharge capacity was retained for B-1, whereas 11.97% was retained for B-2 after the 10th charge-discharge cycle. However, the coulombic efficiency fluctuated and increased after the 10th charge-discharge cycle of both B-1 and B-2 batteries. There are a number of reasons why columbic efficiency exceeds 100%, including an imbalance in the amounts of Li+ absorbed and released, side reactions, and measurement error. This may be due to some structural interruptions that cause an uneven volume of Li+ to be transported. Particularly, the intercalation of less Li+ during charging and the de-intercalation of the maximum volume of Li+ during discharging cause the columbic efficiency to exceed 100%. The repeated occurrence of such phenomena causes the active material to fail and affect the battery's performance adversely [73–75].

It is evident from Figures 7 (a) and (c) that battery B-1 exhibited erratic behavior, and the specific capacities decreased rapidly from the 1st to 10th charge-discharge cycle. Moreover, the specific charge/discharge capacity faded drastically with further cycling, and the battery became out of order. The predominant reason behind this extreme capacity fading is the short-circuiting phenomenon of the battery, as the instantaneous voltage drop occurred from around 1.0 to 0.01V [76,77]. The unanticipated voltage drop is due to the short circuit of the composite Ni-NiO electrodes and the recycled $LiCoO_2$ electrode due to swelling or perforation of the insulating polymeric separator, deflection of electrodes, or presence of impurities in the cell [78]. The incident of the

internal short circuit releases 70% of the battery energy within 60 seconds [79, 80], which causes a rigorous increase in the local temperature that, in turn triggers the chemical side reactions and causes thermal runaway [80]. This short-circuiting tendency became more prominent with further cycling. Hence, long cycling may lead to thermal runway and irreparable cell damage. In contrast, for battery B-2 the charge/discharge curve exhibited improvement as compared to battery B-1 as shown in Figure 7(b). The curve portrayed capacitor-like profiles (no potential flat plateaus); however, a linear variation of the potential in correspondence to the lithium insertion/extraction. This occurrence indicated the pseudo-capacitive behavior, which signifies surface storage nature [81, 82]. The 1st cycle irreversible capacity loss of 21.10% may be ascribed to the formation of a solid electrolyte interface (SEI) caused by the degradation of electrolytes. This irreversible capacity loss gradually dropped to 23.53% after the 10th cycle. The substantial capacity decrease from the 1st to the 10th cycle may be attributed to the structural collapse of the composite by large volume change during cycling, which pointed out the structural inefficiency of the battery. However, the battery capacity retention ability was higher than the previous battery, and therefore, the performance was not worth demonstrating.

### 3.2.2 Electrochemical performance of Ni-NiO composite at 1000$^0$C as anode of LIBs

Figure 8 shows the galvanostatic charge/discharge voltage profiles of battery B-3 in a potential window of 0.01-3.0V Vs. $Li^+$. Interestingly, the initial discharge profile exhibited no obvious plateau region, similar to the typical capacitor-like curve where potential increases/decreases linearly with the lithium insertion/extraction [82]. This occurrence is attributed to the pseudo-capacitive behavior, which indicates the bulk surface storage characteristics [81, 82]. The initial charge curve exhibits higher voltage with two sloping potential ranges at about 2.2 and 2.5V, respectively. The 1st cycle charge-discharge capacities were exhibited as 292.13 and 365.17 mAh $g^{-1}$, respectively. There was an irreversible capacity loss of 18.98% between 1st charge and discharge, which may be connected to the formation of solid electrolyte interface (SEI) and amorphous $Li_2O$ during the discharge process, due to the electrochemically driven electrolyte degradation. It is noted that both the SEI as well as $Li_2O$ are partially decomposed during the subsequent charge process. This irreversibility of SEI and $Li_2O$ formation-decomposition is responsible for the decrease in the charge capacity. The aforementioned occurrence is observed in materials that obey the conversion reaction mechanism [33, 67, 83, 84].

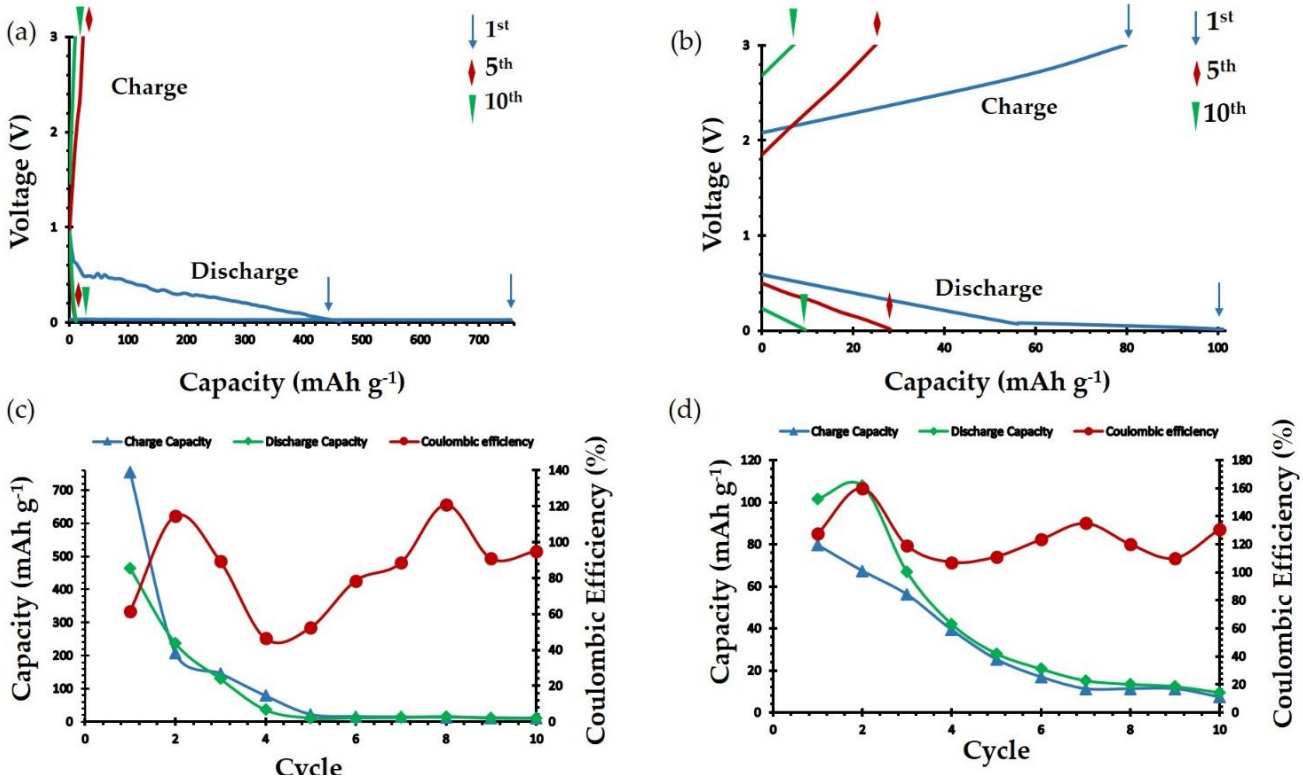


**Figure 7.** (a, b) Charge-Discharge voltage profiles for 1st to 10th cycle; (c, d) Cycle performance and coulombic efficiency at 1C rate for battery B-1 and B-2

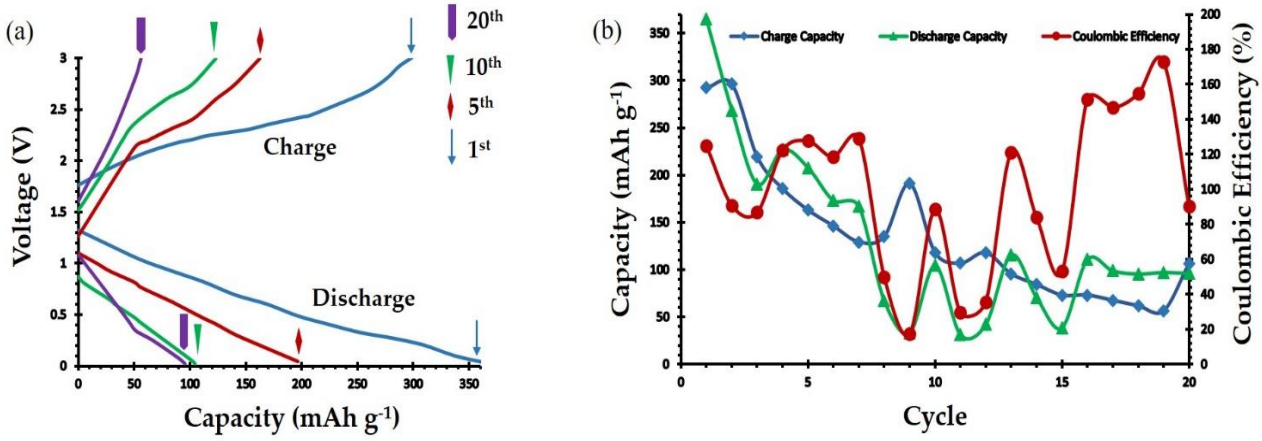


**Figure 8.** (a) Charge-Discharge voltage profiles from 1st to 20th cycle; (b) Cycle performance and coulombic efficiency at 1C rate for battery B-3

In addition, the discharge capacities in the 5th, 10th and 20th cycles have appeared as 196.62 mAh $g^{-1}$, 104.49 mAh $g^{-1}$, and 95.50 mAh $g^{-1}$ respectively with corresponding charge capacities were 162.92 mAh $g^{-1}$, 123.59 mAh $g^{-1}$, and 56.17 mAh $g^{-1}$. The capacities decreased rapidly over cycling and 26.15% of the initial capacity was retained after the 20th cycle for B-3. Moreover, the reversible discharge capacity loss for 1st to 5th, 5th to 10th, 10th to 20th, 1st to 20th were 168.55 mAh $g^{-1}$, 88.13 mAh $g^{-1}$, 8.99 mAh $g^{-1}$, and 269.67 mAh $g^{-1}$, respectively. The average capacity loss per cycle was found to be 13.48 mAh $g^{-1}$ and 26.15% of initial capacity was retained. The initial coulombic efficiency of battery B-3 seemed to be 124.80% at a 1C rate. The coulombic efficiency fluctuated in a random manner throughout the 20 cycles and attained a value of 90.47% after the 20th cycle. The aforementioned performance analysis of B-1, B-2, and B-3 batteries implied that all three batteries are functional and exhibited some capacities with coulombic efficiencies. The charge/discharge profile and cycle performance of B-1 and B-2 clearly indicated the infeasibility of the battery to be employed in practical application. The B-1 battery exhibited an error-prone tendency as an internal short circuit occurred, which was responsible for extreme capacity decay within a few cycles. This may be induced by perforation or crack in the separator, deformity in architecture, and/or defective assembly procedure. In the case of B-2 battery, low capacity resulted from conspicuous surface intercalation, which accounted for structural collapse. However, B-2 battery appeared to have a slight improvement in performance compared to B-1, the battery efficiency, which did not meet expectations. It is noted that the B-3 battery appeared to be a promising one. The B-3 battery exhibited more efficient results than all other batteries, rather it requires high-temperature processing. This may be attributed to the well-ordered and highly crystalline microstructure. Hence, long-term cycling performance has been executed with B-3. As a consequence, more than 40 charge/discharge cycles can be achieved with B-3 at a 1C rate.

Figure 9 exhibits the high cycle charge-discharge profiles for battery B-3 within the voltage window 0.01-3.0V Vs. $Li^+$. The 25th cycle charge-discharge capacities were 73.03 mAh $g^{-1}$ and 112.36 mAh $g^{-1}$. Similarly, the 30th, 35th, and 40th discharge capacities were 98.88 mAh $g^{-1}$, 75.84 mAh $g^{-1}$, and 67.42 mAh $g^{-1}$ respectively with corresponding charge capacities of 61.79 mAh $g^{-1}$, 46.63 mAh $g^{-1}$, and 35.39 mAh $g^{-1}$, respectively. A considerable discharge capacity loss was noticed 13.48 mAh $g^{-1}$ from 25th to 30th cycle. For 30th to 35th, 35th to 40th, and 25th to 40th cycle the discrepancies in discharge capacity became 23.04 mAh $g^{-1}$, 8.42 mAh $g^{-1}$, and 76.97 mAh $g^{-1}$. The average loss in discharge capacity per cycle was 5.13 mAh $g^{-1}$, which was 13.48 mAh $g^{-1}$ for the first 20 cycles. It is noted that discharge capacity loss followed a decreasing trend with an increase in cycle number. Moreover, the battery demonstrated a long-cycle performance and coulombic efficiency at the 1C rate as shown in Figure 9 (a). The coulombic efficiency for the 25th cycle was 95.55%, and the values were 88%, 88.82%, and 100% for 30th, 35th, and 40th cycles. The coulombic efficiency showed a subsequent decrease up to the 35th cycle and attained 100% in the 40th cycle. Furthermore, the retention of initial capacity was 18.46% after the 40th cycle, which was 27.07% and 20.77% for the 30th and 35th cycles. The long-term cycling caused only 7.69% capacity decay from the 20th to 40th cycle. It can be stated that the capacity retention ability manifested a decreasing tendency with cycling. In order to clarify the capacity loss of the as cycled batteries, the surface morphology and elemental analysis of the Ni-NiO composite electrode were performed. It is noted that disassemble of LIBs was performed manually in such a way that the process was not allowed to short-circuit. In addition, Ni-NiO electrode was not washed after disassembling of LIBs, and its original morphology after respective cycling was observed with the presence of an SEI layer. Figure 10 shows the SEM images and EDX spectra of Ni-NiO electrodes of batteries B-1 and B-3 after charge/discharge for 10 and 40 cycles, respectively.

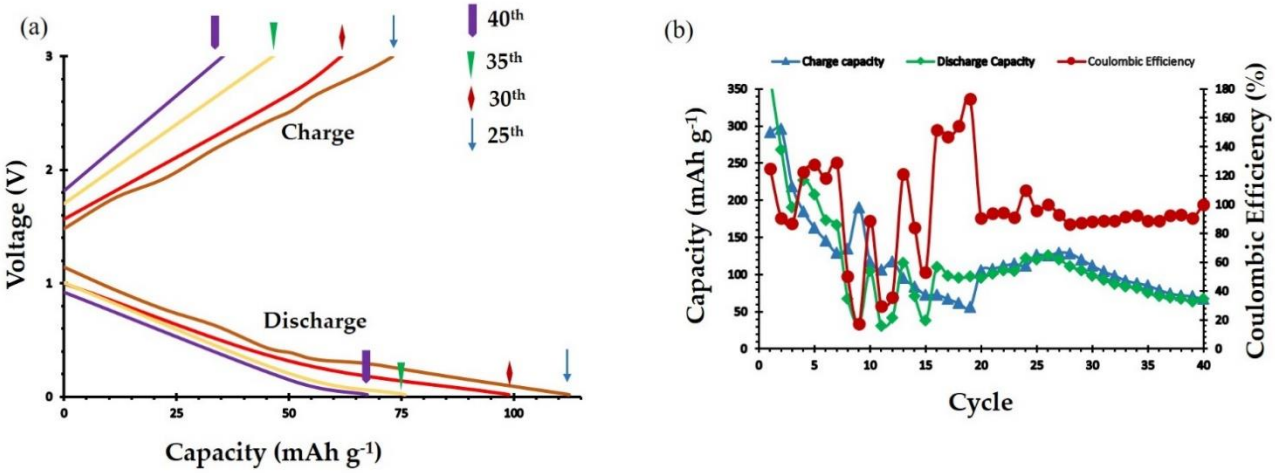


**Figure 9.** (a) Charge-Discharge voltage profiles from 25th to 40th cycle; (b) Long cycle performance and coulombic efficiency at 1C rate for battery B-3

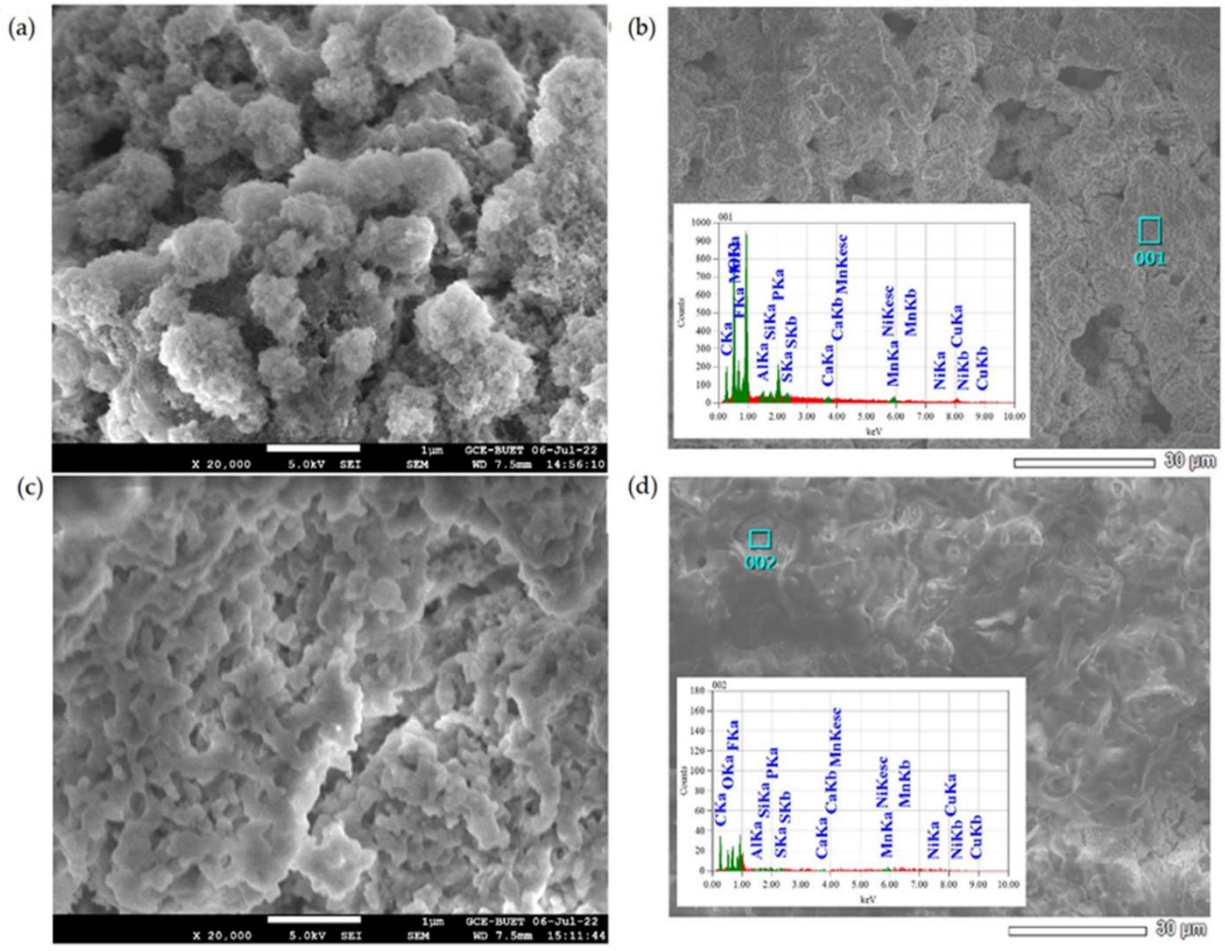


**Figure 10.** SEM and EDX characterization of Ni-NiO electrodes after electrochemical cycling of: (a, b) B-1 and (c, d) B-3

It is noted that the synthesis temperature of electrodes of B-1 and B-3 is 600°C and 1000 °C, respectively. We didn't observe and analyze the SEM images and EDX spectra of the electrode of B-2, which was synthesized at 800°C due to the similar electrochemical performances of B-1. The initial microstructure of Ni-NiO electrode of B-1 enormously changed to agglomerated and cracked surface, as shown in Figure 10(a). It is noted that the width of some cracks increased and subsequently crushed due to the volume change of NiO and came off the current collector, leading to the drastic capacity fade of B-1. However, the original pebble stone microstructure of Ni-NiO electrode of B-3 entirely changed to a compressed honeycomb-like structure, as shown in Figure 10(c). It is noted that these both electrodes exhibited different morphology with few nanometer diameter pores after charge/discharge cycles at 1 C current rate. This could be attributed by the structural change during the first lithiation process when NiO structure converted to Ni nanoparticle inside $Li_2O$ and gel-like matrixes [17, 29, 85]. A similar morphological change is observed in NiO electrode as anode after the electrochemical cycling of LIBs [23, 78, 84]. It is noted that the decomposition of electrolyte is substantial, which can be another reason for the drastic capacity fading of Ni-NiO. The EDX spectra of Ni-NiO electrodes after 10 and 40 charge/discharge cycles are shown in Figures 10 (b) and (d), respectively. It is observed that the presence of elements fluorine (F) and phosphorus (P) is due to the decomposition of $LiPF_6$ along with the impurities elements of manganese (Mn), calcium (Ca), silicon (Si), and sulfur (S). In addition, carbon (C) is observed due to the decomposition of carbonate-based organic solvents. A similar decomposition phenomenon was observed in carbonate-based lithium salt electrolytes such as 1.2 M $LiPF_6$/EC [86], 1 M $LiPF_6$/EC-DEC [87], and 1 M $LiPF_6$/EC-DEC-DMC [88]. From the above discussion, it can be noted that the B-3 has appeared as the propitious one among other batteries. It is noted that the synthesis required high-temperature ($1000^0$C) processing; however, it exhibited noteworthy performance. The contribution of this specific research is to establish a convenient synthesis technique and undoubtedly unique architecture. In addition, the battery assembly operation was simple without any glovebox facility. The achieved capacity is lower than the NiO itself and other nanostructures; however, higher than the practical capacity of graphite anode. Moreover, replacing graphite with Ni-NiO composite will eliminate the safety issues regarding graphite anode with considerably high specific capacity. Furthermore, the remarkable performance stimulated the execution as a battery anode in practical application with no probable hazard.

## 4. Conclusions

In summary, we have fabricated microstructured composite of Ni-NiO through a simple and single-step thermal oxidation approach and subsequent mechanical ball milling process. At three distinct temperatures- 600˚C, 800˚C, and 1000˚C oxidation of Ni powder was performed. The as-synthesized microstructured composite of Ni-NiO was employed as an anode of LIBs, and the following conclusions are drawn from this study:

- It was observed that the electrode synthesized at 600˚C (B-1) delivered a discharge and charge capacity of 464.04 mAh $g^{-1}$ and 754.49 mAh $g^{-1}$ during 1st cycle which decreased drastically to 10.67 mAh $g^{-1}$ and 10.11 mAh $g^{-1}$ after 10th cycle at 1C rate. This electrode experiences an internal short circuit, which was the major reason behind the capacity fading. Moreover, the insufficient active nanoparticle loading in the electrode causes less reaction with lithium. However, the high elasticity of the electrode causes ease of electrolyte and ion access, and the brittleness of the electrode causes severe volume expansion and structural degradation of the electrode within 10 cycles.
- The electrode synthesized at 800˚C (B-2) exhibited a specific discharge-charge capacity of 101.12 mAh $g^{-1}$ and 79.77 mAh $g^{-1}$ during 1st cycle and faded rapidly to 9.55 mAh $g^{-1}$ and 7.30 mAh $g^{-1}$ after the 10th cycle. Though irreversible capacity loss decreases from the previous electrode, the electrode cannot sustain long cycling. The more reversible capacity was due to the presence of Ni nanoparticles, possessing catalytic activity, facilitating the decomposition of $Li_2O$ and SEI layer during the charging process. However, the amount of active nanoparticles on the electrode increases with temperature increase, the electrode elasticity, and brittleness decrease, and the electrode was unable to buffer the volume-induced stress that resulted in the crack on the surface and structural degradation of the electrode.
- One of the best electrochemical performances was observed in the electrode synthesized at 1000˚C temperature (B-3). The electrode delivered a specific discharge and charge capacity of 365.17 mAh $g^{-1}$ and 298.85 mAh $g^{-1}$ during 1st cycle. A reversible capacity of 67.41 mAh $g^{-1}$ was achieved after the 40th cycle at a 1C rate. The discharge/charge capacity fluctuated randomly up to the 20th cycle as the electrode material became more ductile due to temperature increase, which impedes the smooth insertion of $Li^+$. During continuous charging/discharging, the rapid lithium insertion/de-insertion causes active electrode materials to get pulverized. After the 20th cycle, the electrode capacity fluctuated systematically and retained 18.46% initial capacity with coulombic efficiency of 100% after the 40th cycle. This may be due to continuous cycling; the structural reconstruction of the electrode causes a reduction in particle size of active material, and thus, nano-crystallization improves the cycling performance. The prolonged cycling causes pulverization of the electrode, the active materials detached from the current collector, and the failure occurs.

**Ethical issue**

The authors are aware of and comply with best practices in publication ethics, specifically with regard to authorship (avoidance of guest authorship), dual submission, manipulation of figures, competing interests, and compliance with policies on research ethics. The authors adhere to publication requirements that the submitted work is original and has not been published elsewhere.

**Data availability statement**
The manuscript contains all the data. However, more data will be available upon request from the authors.

**Conflict of interest**
The authors declare no potential conflict of interest.

**Funding**
This work is co-supported by Chittagong University of Engineering & Technology (CUET), Bangladesh, through research grant no. CUET/CHSR-35/17(iii), University Grants Commission of Bangladesh-grant no. 37.01. 0000.73.06.065.22.1607, and a grant (No. JB230001) from the Korea Institute of Industrial Technology (KITECH). The corresponding author is responsible for ensuring that the descriptions are accurate and agreed upon by all authors.

**References**

[1] Zhang J, Terrones M, Park CR, Mukherjee R, Monthioux M, Koratkar N, et al. Carbon science in 2016: Status, challenges and perspectives. Vol. 98, Carbon. Elsevier Ltd; 2016. p. 708–32.
[2] Chemistry of Materials Editorial. Available from: https://doi.org/10.1021/acs.chemmater.
[3] Rodrigues MTF, Babu G, Gullapalli H, Kalaga K, Sayed FN, Kato K, et al. A materials perspective on Li-ion batteries at extreme temperatures. Nat Energy. 2017 Aug;2(8).
[4] Rahman MdA, Kim J, Hossain S. Recent advances of energy storage technologies for grid: A comprehensive review. Energy Storage. 2022 Jan 10;
[5] Nardo M, Saisana M, Saltelli A, Tarantola S, Hoffman H, Giovannini E. Handbook on constructing composite indicators: methodology and user guide. Organisation for Economic Cooperation and Development (OECD). Statistics Working Paper JT00188147, OECD, France. 2005;
[6] Winter M, Besenhard JO, Spahr ME, Novμk P. Insertion Electrode Materials for Rechargeable Lithium Batteries. https://doi.org/10.1002/(SICI)1521-4095(199807)10:10<725::AID-ADMA725>3.0.CO;2-Z
[7] Van Schalkwijk WA, Scrosati B. Advances in Lithium-ion Batteries Kluwer Academic. Plenum, New York; 2002.
[8] Ma D, Cao Z, Hu A. Si-based anode materials for li-ion batteries: A mini review. Vol. 6, Nano-Micro Letters. Shanghai Jiaotong University; 2014. p. 347–58.
[9] An Q, Lv F, Liu Q, Han C, Zhao K, Sheng J, et al. Amorphous vanadium oxide matrixes supporting hierarchical porous Fe3O4/graphene nanowires as a high-rate lithium storage anode. Nano Lett. 2014 Nov 12;14(11):6250–6.
[10] Dai R, Wang Y, Da P, Wu H, Xu M, Zheng G. Indirect growth of mesoporous Bi@C core-shell nanowires for enhanced lithium-ion storage. Nanoscale. 2014 Nov 7;6(21):13236–41.
[11] Yang C, Jiang Y, Liu X, Zhong X, Yu Y. Germanium encapsulated in sulfur and nitrogen co-doped 3D porous carbon as an ultra-long-cycle life anode for lithium ion batteries. J Mater Chem A Mater. 2016;4(48):18711–6.
[12] Choi JW, Aurbach D. Promise and reality of post-lithium-ion batteries with high energy densities. Vol. 1, Nature Reviews Materials. Nature Publishing Group; 2016.
[13] Chan CK, Ruffo R, Hong SS, Cui Y. Surface chemistry and morphology of the solid electrolyte interphase on silicon nanowire lithium-ion battery anodes. J Power Sources. 2009;189(2):1132–40.
[14] Ruffo R, Hong SS, Chan CK, Huggins RA, Cui Y. Impedance analysis of silicon nanowire lithium ion battery anodes. The Journal of Physical Chemistry C. 2009;113(26):11390–8.
[15] Li, Si. 648 wileyonlinelibrary.com [Internet]. 2015. Available from: www.MaterialsViews.com
[16] Ferg E, Gummow RJ d, De Kock A, Thackeray MM. Spinel anodes for lithium-ion batteries. J Electrochem Soc. 1994;141(11):L147.
[17] Zhao Y, Li X, Yan B, Xiong D, Li D, Lawes S, et al. Recent Developments and Understanding of Novel Mixed Transition-Metal Oxides as Anodes in Lithium Ion Batteries. Vol. 6, Advanced Energy Materials. Wiley-VCH Verlag; 2016.
[18] Li T, Li X, Wang Z, Guo H, Li Y, Wang J. A new design concept for preparing nickel-foam-supported metal oxide microspheres with superior electrochemical properties. J Mater Chem A Mater. 2017;5(26):13469–74.
[19] Hao L, Liang M, Weiwei S, Yong W. Bimetal-Organic Framework: One-Step Homogenous Formation and its Derived Mesoporous Ternary Metal Oxide Nanorod for High-Capacity, High-Rate, and Long-Cycle-Life Lithium Storage. Adv Funct Mater. 2016 Feb 16;26(7):1098–103.
[20] Chen Z, Zhou M, Cao Y, Ai X, Yang H, Liu J. In situ generation of few-layer graphene coatings on SnO 2-SiC core-shell nanoparticles for high-performance lithium-ion storage. Adv Energy Mater. 2012 Jan;2(1):95–102.
[21] Liu H, Wang G, Liu J, Qiao S, Ahn H. Highly ordered mesoporous NiO anode material for lithium ion batteries with an excellent electrochemical performance. J Mater Chem. 2011 Mar 7;21(9):3046–52.
[22] Rahman MA, Wong YC, Song G, Zhu DM, Wen C. Improvement on electrochemical performances of nanoporous titania as anode of lithium-ion batteries through annealing of pure titanium foils. Journal of Energy Chemistry. 2018 Jan 1;27(1):250–63.
[23] Rahman MA, Wen C. Nanogravel structured NiO/Ni foam as electrode for high-performance lithium-ion batteries. Ionics (Kiel). 2015 Oct 22;21(10):2709–23.
[24] Zhu Y, Choi SH, Fan X, Shin J, Ma Z, Zachariah MR, et al. Recent Progress on Spray Pyrolysis for High Performance Electrode Materials in Lithium and Sodium Rechargeable Batteries. Vol. 7, Advanced Energy Materials. Wiley-VCH Verlag; 2017.
[25] Cai Z, Xu L, Yan M, Han C, He L, Mulonda Hercule K, et al. Manganese Oxide/Carbon Yolk-Shell Nanorod Anodes for High Capacity Lithium Batteries [Internet]. 2014. Available from: http://pubs.acs.org

[26] Wang Y, Xu J, Wu H, Xu M, Peng Z, Zheng G. Hierarchical SnO 2-Fe 2O 3 heterostructures as lithium-ion battery anodes. J Mater Chem. 2012 Nov 7;22(41):21923–7.

[27] Rahman MA, Wong YC, Song G, Wen C. A review on porous negative electrodes for high performance lithium-ion batteries. Journal of Porous Materials. 2015 Oct 7;22(5):1313–43.

[28] Sun MH, Huang SZ, Chen LH, Li Y, Yang XY, Yuan ZY, et al. Applications of hierarchically structured porous materials from energy storage and conversion, catalysis, photocatalysis, adsorption, separation, and sensing to biomedicine. Chem Soc Rev. 2016 Jun 21;45(12):3479–563.

[29] Zheng M, Tang H, Li L, Hu Q, Zhang L, Xue H, et al. Hierarchically nanostructured transition metal oxides for lithium-ion batteries. Advanced Science. 2018;5(3):1700592.

[30] Kumar Rai A, Tuan Anh L, Park CJ, Kim J. Electrochemical study of NiO nanoparticles electrode for application in rechargeable lithium-ion batteries. Ceram Int. 2013 Aug;39(6):6611–8.

[31] Li X, Dhanabalan A, Wang C. Enhanced electrochemical performance of porous NiO-Ni nanocomposite anode for lithium ion batteries. J Power Sources. 2011 Nov 15;196(22):9625–30.

[32] Rahman MA, Zhu X, Wen C. Fabrication of Nanoporous Ni by Chemical Dealloying Al from Ni-Al Alloys for Lithium-ion Batteries [Internet]. Vol. 10, Int. J. Electrochem. Sci. 2015. Available from: www.electrochemsci.org

[33] Wang C, Wang D, Wang Q, Chen H. Fabrication and lithium storage performance of three-dimensional porous NiO as anode for lithium-ion battery. J Power Sources. 2010 Nov 1;195(21):7432–7.

[34] Kim GP, Park S, Nam I, Park J, Yi J. Synthesis of porous NiO materials with preferentially oriented crystalline structures with enhanced stability as lithium ion battery anodes. J Power Sources. 2013;237:172–7.

[35] Du M, Li Q, Pang H. Oxalate-derived porous prismatic nickel/nickel oxide nanocomposites toward lithium-ion battery. J Colloid Interface Sci. 2020 Nov 15;580:614–22.

[36] Singh J, Lee S, Kim S, Singh SP, Kim J, Rai AK. Fabrication of 1D mesoporous NiO nano-rods as high capacity and long-life anode material for lithium ion batteries. J Alloys Compd. 2021 Jan 5;850.

[37] Duraisamy E, Sujithkrishnan E, Kannadasan K, Prabunathan P, Elumalai P. Facile metal complex-derived Ni/NiO/Carbon composite as anode material for Lithium-ion battery. Journal of Electroanalytical Chemistry. 2021 Apr 15;887.

[38] Cheng CF, Chen YM, Zou F, Yang KC, Lin TY, Liu K, et al. Nanoporous gyroid Ni/NiO/C nanocomposites from block copolymer templates with high capacity and stability for lithium storage. J Mater Chem A Mater. 2018;6(28):13676–84.

[39] Liu L, Li Y, Yuan S, Ge M, Ren M, Sun C, et al. Nanosheet-based NiO microspheres: Controlled solvothermal synthesis and Lithium storage performances. Journal of Physical Chemistry C. 2010 Jan 14;114(1):251–5.

[40] Jae W, Song J, Hong JJ, Kim J. Raspberry-like hollow Ni/NiO nanospheres anchored on graphitic carbon sheets as anode material for lithium-ion batteries. J Alloys Compd. 2019 Oct 15;805:957–66.

[41] Varghese B, Reddy M V., Yanwu Z, Lit CS, Hoong TC, Rao GVS, et al. Fabrication of NiO nanowall electrodes for high performance lithium ion battery. Chemistry of Materials. 2008 May 27;20(10):3360–7.

[42] Bell J, Ye R, Ahmed K, Liu C, Ozkan M, Ozkan CS. Free-standing Ni-NiO nanofiber cloth anode for high capacity and high rate Li-ion batteries. Nano Energy. 2015 Nov 1;18:47–56.

[43] Liu L, Guo Y, Wang Y, Yang X, Wang S, Guo H. Hollow NiO nanotubes synthesized by bio-templates as the high performance anode materials of lithium-ion batteries. Electrochim Acta. 2013;114:42–7.

[44] Wu MS, Lin YP. Monodispersed macroporous architecture of nickel-oxide film as an anode material for thin-film lithium-ion batteries. Electrochim Acta. 2011 Feb 1;56(5):2068–73.

[45] Su D, Kim HS, Kim WS, Wang G. Mesoporous nickel oxide nanowires: Hydrothermal synthesis, characterisation and applications for lithium-ion batteries and supercapacitors with superior performance. Chemistry - A European Journal. 2012 Jun 25;18(26):8224–9.

[46] Pang Y, Zhang J, Chen D, Jiao X. 3D hierarchical porous NiO nanoflowers as an advanced anode material with remarkable lithium storage performance. RSC Adv. 2016;6(36):30395–400.

[47] Jadhav HS, Thorat GM, Mun J, Seo JG. Self-assembled hierarchical 3D - NiO microspheres with ultra-thin porous nanoflakes for lithium-ion batteries. J Power Sources. 2016 Jan 20;302:13–21.

[48] Yuan YF, Xia XH, Wu JB, Yang JL, Chen YB, Guo SY. Hierarchically ordered porous nickel oxide array film with enhanced electrochemical properties for lithium ion batteries. Electrochem commun. 2010 Jul;12(7):890–3.

[49] Zhu X, Luo B, Butburee T, Zhu J, Han S, Wang L. Hierarchical macro/mesoporous NiO as stable and fast-charging anode materials for lithium-ion batteries. Microporous and Mesoporous Materials. 2017 Jan 15;238:78–83.

[50] Li Q, Yi Z, Cheng Y, Wang XX, Yin D, Wang L. Microwave-assisted synthesis of the sandwich-like porous Al 2 O 3 /RGO nanosheets anchoring NiO nanocomposite as anode materials for lithium-ion batteries. Appl Surf Sci. 2018 Jan 1;427:354–62.

[51] Wang X, Yang Z, Sun X, Li X, Wang D, Wang P, et al. NiO nanocone array electrode with high capacity and rate capability for Li-ion batteries. J Mater Chem. 2011 Jul 21;21(27):9988–90.

[52] Li T, Ni S, Lv X, Yang X, Duan S. Preparation of NiO-Ni/natural graphite composite anode for lithium ion batteries. J Alloys Compd. 2013 Mar 15;553:167–71.

[53] Zhu XJ, Hu J, Dai HL, Ding L, Jiang L. Reduced graphene oxide and nanosheet-based nickel oxide microsphere composite as an anode material for

lithium ion battery. Electrochim Acta. 2012 Mar 1;64:23–8.
[54] Mai YJ, Tu JP, Gu CD, Wang XL. Graphene anchored with nickel nanoparticles as a high-performance anode material for lithium ion batteries. J Power Sources. 2012 Jul 1;209:1–6.
[55] Qiu Y, Huang H, Song W, Gan Y, Wang K, Zhang J, et al. In-situ electrolytic synthesis and superior lithium storage capability of Ni–NiO/C nanocomposite by sacrificial nickel anode in molten carbonates. J Alloys Compd. 2020 Sep 5;834.
[56] Huang XH, Tu JP, Xia XH, Wang XL, Xiang JY, Zhang L. Porous NiO/poly(3,4-ethylenedioxythiophene) films as anode materials for lithium ion batteries. J Power Sources. 2010 Feb 15;195(4):1207–10.
[57] Huang XH, Tu JP, Xia XH, Wang XL, Xiang JY. Nickel foam-supported porous NiO/polyaniline film as anode for lithium ion batteries. Electrochem commun. 2008 Sep;10(9):1288–90.
[58] Rahman MdA, Rahman MdM, Song G. A review on binder-free NiO-Ni foam as anode of high performance lithium-ion batteries . Energy Storage. 2021 Aug 13;
[59] Sarker B, Rahman MA, Rahman MM, Islam MS. Fabrication of ni-nio foams by powder metallurgy technique and study of bulk crushing strength. Trends in Sciences. 2021 Dec 1;18(23).
[60] Cabanas-Polo S, Bermejo R, Ferrari B, Sanchez-Herencia AJ. Ni-NiO composites obtained by controlled oxidation of green compacts. Corros Sci. 2012 Feb;55:172–9.
[61] Xia Q, Zhao H, Teng Y, Du Z, Wang J, Zhang T. Synthesis of NiO/Ni nanocomposite anode material for high rate lithium-ion batteries. Mater Lett. 2015 Mar 1;142:67–70.
[62] Huang XH, Tu JP, Zhang CQ, Xiang JY. Net-structured NiO–C nanocomposite as Li-intercalation electrode material. Electrochem commun [Internet]. 2007;9(5):1180–4. Available from: https://www.sciencedirect.com/science/article/pii/S1388248107000185
[63] Zhu H, Zeng X, Han T, Li X, Zhu S, Sun B, et al. A nickel oxide nanoflakes/reduced graphene oxide composite and its high-performance lithium-storage properties. Journal of Solid State Electrochemistry. 2019 Jul 19;23(7):2173–80.
[64] Xu C, Sun J, Gao L. Large scale synthesis of nickel oxide/multiwalled carbon nanotube composites by direct thermal decomposition and their lithium storage properties. J Power Sources. 2011 Jun 1;196(11):5138–42.
[65] Yu Y, Gu L, Zhu C, Tsukimoto S, Van Aken PA, Maier J. Reversible storage of lithium in silver-coated three-dimensional macroporous silicon. Advanced materials. 2010;22(20):2247–50.
[66] Huang XH, Tu JP, Zhang B, Zhang CQ, Li Y, Yuan YF, et al. Electrochemical properties of NiO-Ni nanocomposite as anode material for lithium ion batteries. J Power Sources. 2006 Oct 20;161(1):541–4.
[67] Ni S, Li T, Lv X, Yang X, Zhang L. Designed constitution of NiO/Ni nanostructured electrode for high performance lithium ion battery. Electrochim Acta. 2013 Feb 28;91:267–74.
[68] Oh SW, Bang HJ, Bae YC, Sun YK. Effect of calcination temperature on morphology, crystallinity and electrochemical properties of nano-crystalline metal oxides (Co3O4, CuO, and NiO) prepared via ultrasonic spray pyrolysis. J Power Sources. 2007;173(1):502–9.
[69] Werber T. Joining of nickel powder grains by thermal oxidation. Vol. 42, Solid State Ionics. 1990. https://doi.org/10.1016/0167-2738(90)90009-G
[70] Hernández N, Moreno R, Sánchez-Herencia AJ, Fierro JLG. Surface behavior of nickel powders in aqueous suspensions. J Phys Chem B. 2005;109(10):4470–4.
[71] Evans HE. Stress effects in high temperature oxidation of metals. International materials reviews. 1995;40(1):1–40.
[72] Clarke DR. S tress generation during high-temperature oxidation of metallic alloys. Vol. 6, Current Opinion in Solid State and Materials Science. 2002.
[73] Huang Y, Sun W, Xu K, Zhang J, Zhang H, Li J, et al. Robust interphase on both anode and cathode enables stable aqueous lithium-ion battery with coulombic efficiency exceeding 99%. Energy Storage Mater. 2022;46:577–82.
[74] Wang Z, Zhang P, Li J, Zhang C, Jiang JX, Lv M, et al. A low-cost naphthaldiimide based organic cathode for rechargeable lithium-ion batteries. Front Chem. 2022;10.
[75] Yasin G, Arif M, Ma J, Ibraheem S, Yu D, Zhang L, et al. Self-templating synthesis of heteroatom-doped large-scalable carbon anodes for high-performance lithium-ion batteries. Inorg Chem Front. 2022;9(6):1058–69.
[76] Lee SH, Harding JR, Liu DS, D'Arcy JM, Shao-Horn Y, Hammond PT. Li-anode protective layers for Li rechargeable batteries via layer-by-layer approaches. Chemistry of Materials. 2014;26(8):2579–85.
[77] Zhao W, Luo G, Wang CY. Modeling nail penetration process in large-format Li-ion cells. J Electrochem Soc. 2014;162(1): A207.
[78] Rahman MA, Wen C. A study of the capacity fade of porous NiO/Ni foam as negative electrode for lithium-ion batteries. Ionics (Kiel). 2016 Feb 1;22(2):173–84.
[79] Maleki H, Howard JN. Internal short circuit in Li-ion cells. J Power Sources. 2009;191(2):568–74.
[80] Cai W, Wang H, Maleki H, Howard J, Lara-Curzio E. Experimental simulation of internal short circuit in Li-ion and Li-ion-polymer cells. J Power Sources. 2011;196(18):7779–83.
[81] Li B, Zhang H, Wang D, Lv H, Zhang C. Agricultural waste-derived activated carbon for high performance lithium-ion capacitors. RSC Adv. 2017;7(60):37923–8.
[82] Hosono E, Matsuda H, Honma I, Ichihara M, Zhou H. High-Rate Lithium Ion Batteries with Flat Plateau Based on Self-Nanoporous Structure of Tin Electrode. J Electrochem Soc. 2007;154(2): A146.

[83] Huang XH, Tu JP, Zhang CQ, Zhou F. Hollow microspheres of NiO as anode materials for lithium-ion batteries. Electrochim Acta. 2010 Dec 1;55(28):8981–5.

[84] Poizot P, Laruelle S, Grugeon S, Dupont L, Tarascon JM. Nano-sized transition-metal oxides as negative-electrode materials for lithium-ion batteries. Nature. 2000;407(6803):496–9.

[85] Jin J, Wu L, Huang S, Yan M, Wang H, Chen L, et al. Hierarchy Design in Metal Oxides as Anodes for Advanced Lithium-Ion Batteries. Small Methods. 2018;2(11):1800171.

[86] Nie M, Chalasani D, Abraham DP, Chen Y, Bose A, Lucht BL. Lithium ion battery graphite solid electrolyte interphase revealed by microscopy and spectroscopy. The Journal of Physical Chemistry C. 2013;117(3):1257–67.

[87] Aurbach D, Ein-Eli Y, Markovsky B, Zaban A, Luski S, Carmeli Y, et al. The study of electrolyte solutions based on ethylene and diethyl carbonates for rechargeable Li batteries: II. Graphite electrodes. J Electrochem Soc. 1995;142(9):2882.

[88] Lu M, Cheng H, Yang Y. A comparison of solid electrolyte interphase (SEI) on the artificial graphite anode of the aged and cycled commercial lithium ion cells. Electrochim Acta. 2008;53(9):3539–46.